



AIAA-2003-0684

Simultaneous MHz Rate Flow Visualization and Wavefront Sensing for Aero-Optics

B. Thurow, M. Samimy and W. Lempert
The Ohio State University

S.R. Harris
Air Force Research Laboratory, Sensors Directorate

J. Widiker and B. Duncan
University of Dayton

**41st AIAA Aerospace Sciences Meeting and
Exhibit**

January 6-9, 2003/ Reno, NV

Report Documentation Page				Form Approved OMB No. 0704-0188	
Public reporting burden for the collection of information is estimated to average 1 hour per response, including the time for reviewing instructions, searching existing data sources, gathering and maintaining the data needed, and completing and reviewing the collection of information. Send comments regarding this burden estimate or any other aspect of this collection of information, including suggestions for reducing this burden, to Washington Headquarters Services, Directorate for Information Operations and Reports, 1215 Jefferson Davis Highway, Suite 1204, Arlington VA 22202-4302. Respondents should be aware that notwithstanding any other provision of law, no person shall be subject to a penalty for failing to comply with a collection of information if it does not display a currently valid OMB control number.					
1. REPORT DATE JAN 2003		2. REPORT TYPE		3. DATES COVERED 00-00-2003 to 00-00-2003	
4. TITLE AND SUBTITLE Simultaneous MHz Rate Flow Visualization and Wavefront Sensing for Aero-Optics				5a. CONTRACT NUMBER	
				5b. GRANT NUMBER	
				5c. PROGRAM ELEMENT NUMBER	
6. AUTHOR(S)				5d. PROJECT NUMBER	
				5e. TASK NUMBER	
				5f. WORK UNIT NUMBER	
7. PERFORMING ORGANIZATION NAME(S) AND ADDRESS(ES) Ohio State University, Department of Mechanical Engineering, Columbus, OH, 43210				8. PERFORMING ORGANIZATION REPORT NUMBER	
9. SPONSORING/MONITORING AGENCY NAME(S) AND ADDRESS(ES)				10. SPONSOR/MONITOR'S ACRONYM(S)	
				11. SPONSOR/MONITOR'S REPORT NUMBER(S)	
12. DISTRIBUTION/AVAILABILITY STATEMENT Approved for public release; distribution unlimited					
13. SUPPLEMENTARY NOTES					
14. ABSTRACT					
15. SUBJECT TERMS					
16. SECURITY CLASSIFICATION OF:			17. LIMITATION OF ABSTRACT Same as Report (SAR)	18. NUMBER OF PAGES 15	19a. NAME OF RESPONSIBLE PERSON
a. REPORT unclassified	b. ABSTRACT unclassified	c. THIS PAGE unclassified			

Simultaneous MHz Rate Flow Visualization and Wavefront Sensing for Aero-Optics

Brian Thurow, Mo Samimy¹ and Walter Lempert
The Ohio State University

Scott Harris
Air Force Research Laboratory, Sensors Directorate

Jeff Widiker and Bradley Duncan
University of Dayton

Newly developed optical diagnostic techniques are used to examine the temporal evolution of wavefront aberrations imposed upon an optical beam as it passes through a rectangular compressible turbulent jet. A recently developed MHz rate system based on a pulse burst laser and ultra high-speed CCD camera is used for flow visualization. A newly developed two-dimensional MHz rate Shack-Hartman wavefront sensor is used to measure the wavefront distortion. The wavefront sensor consists of a HeNe laser, a micro-lens array and an ultra high-speed camera. The MHz rate flow visualization and wavefront sensing are used simultaneously to investigate the aero-optic effects of an ideally expanded, high Reynolds number, Mach 1.3 rectangular jet. Preliminary results are presented that show the potential of the technique to acquire time-resolved two-dimensional wavefront data with detailed aero-optic effects. A number of improvements to the technique that will be used in future work are also discussed.

I. Introduction

The application of lasers in modern military aircraft is continuously growing as we search for more accurate and effective means of targeting, sensing and energy delivery. Laser targeting systems for 'smart' bombs, laser radar and imaging devices, and the airborne laser weapon system are typical examples of lasers used in modern aircraft. The performance of these devices, however, heavily depends on the wavefront degradation that occurs as the laser beam exits through the turbulent flow over the transmission window on the aircraft. Depending on the beam size relative to the turbulence scales in the flow, this degradation results in adverse effects such as defocus, beam jitter and beam steering (Cassady et al., 1989). The study of this flow-induced degradation is termed aero-optics.

The ultimate goal of aero-optics research is to understand the connection between a flow field and the associated optical degradation well enough so that

correction schemes can be applied to minimize the adverse effects and prediction capabilities can be developed to take into account optical degradation effects. There has been much effort and success when dealing with problems of optical propagation through the atmosphere (e.g. ground based telescopes, etc.), but very little progress has been made for flow fields typical of modern aircraft (Jumper and Fitzgerald, 2002). These flow fields are typically compressible with turbulence features characterized by a wide range of spatial and temporal scales.

For practical flow fields, the temporal bandwidth can be from a few up to several 100's of kHz while the spatial scale must at a very minimum be on the order of the large-scale features of the flow. Until recently, high spatial and temporal bandwidth wavefront measurements had not been simultaneously achievable. Hugo et al. (1997) have demonstrated a small aperture beam technique that can resolve an optical wavefront at multiple points in space (~ 5) at a rate of up to 100 kHz, thus simultaneously achieving a high temporal bandwidth and a modest spatial resolution. This data was then subsequently used to develop a model for the index of refraction field of a weakly compressible flow field (Fitzgerald and Jumper, 2002). The technique is currently limited by the number of sensors that can be operated simultaneously and has only been used for one-dimensional wavefront reconstructions. Practical

¹Corresponding author: Samimy.1@osu.edu

flow fields, however, are quite three-dimensional and cause two-dimensional wavefront degradation, which necessitates a two-dimensional wavefront sensor.

One device capable of measuring a two-dimensional wavefront is a Shack-Hartman (SH) wavefront sensor. In a SH sensor, the wavefront is spatially discretized into a grid pattern by a lenslet array. The displacement of each focal spot is related to the mean tilt (slope) of the wavefront across the aperture of the corresponding lenslet. The basic concept is shown in Figure 1 and described by

$$\theta \approx \tan \theta = \frac{\delta}{f} \quad (1)$$

where θ is the angle of the incident wavefront, δ is the deflection of a spot, and f is the focal length of the lens.

If the spatial sampling of the wavefront is sufficiently fine such that the wavefront is approximately linear within each sampled area, an array of diffraction limited spots will be produced by the lenslet array. The array of spots can be recorded by a CCD camera. The associated spot displacements can then be measured directly from the recorded spot pattern.

As will be discussed, the main limiting factor in a SH sensor is the recording medium and its spatial and temporal constraints. In an effort to increase the speed of a SH sensor, McMackin et al. (1995) used a cylindrical lens array and a 1-D CCD camera. They were able to achieve speeds in excess of 2 kHz, but only could resolve a 1-D wavefront. Recent advances in CCD technology have made available a high-speed 2-D camera with moderate spatial resolution. This technology is utilized in this work to create a high-speed (1 MHz) 2-D SH sensor.

In conjunction with a high-speed wavefront sensor, a high-speed flow diagnostic tool is needed to relate the flow field to the optical aberrations. Thurow et al. (2002a&b) have demonstrated a MHz rate flow visualization technique and applied it to Mach 1.3 and 2.0 axisymmetric jets. The technique uses a custom built pulse burst laser and an ultra high-speed digital camera to visualize the flow. It can take 17 images of the flow at up to a 1 MHz rate. In their work, they were able to visualize structures undergoing such events as tearing and pairing. They also were able to measure the convective velocity of structures.

The index of refraction is related to the flow field through

$$n = 1 + K\rho \quad (2)$$

where K is the Gladstone-Dale constant ($2.23 \times 10^{-4} \text{ m}^3/\text{kg}$ for air) and ρ is the density in kg/m^3 . Thus, the wavefront can be calculated directly from the density

field of the flow. Dimotakis et al. (2001) utilized Rayleigh scattering to measure a 2-D density field of an incompressible shear layer and calculated the aberrated 1-D wavefront passed through the flow field. They showed that a simplified model for the index of refraction field using only the boundaries of the mixing layer gave an accurate representation of the wavefront and greatly simplified the flow diagnostic requirements. Their technique, however, was limited to instantaneous snapshots of the flow.

The overall goal of this project is to apply the latest advances in laser and camera technology to the problem of aero-optics. Specifically, we are using the MHz rate flow visualization in conjunction with a MHz rate SH wavefront sensor to study the effect of a high Reynolds number compressible flow field on a wavefront passing through it. This study should increase our understanding of the connection between turbulence structures and optical aberrations in compressible flow fields and provide a database of information that can be exploited by modelers and designers of aircraft systems incorporating lasers.

At this point, the project is in its early stages and only its initial development is discussed in this paper. Specifically, this paper describes a set of preliminary experiments designed to test and validate the techniques used. These experiments involve the application of the MHz rate flow visualization system and a newly developed SH wavefront sensor to the problem of an optical beam passing through a Mach 1.3 rectangular jet flow. Section II describes the MHz rate flow visualization technique and preliminary efforts to predict the wavefront from the flow visualization images. Section III discusses the development of the MHz rate SH wavefront sensor and its limitations and potential. Section IV details the application of both techniques simultaneously to a Mach 1.3 rectangular jet and discusses some preliminary connections that can be made between flow structure and optical aberrations. Section V points out a number of items that will be implemented in the next phase of the research that should greatly improve the quality of data acquired. Lastly, Section VI draws some conclusions based on the preliminary results.

II. MHz rate flow visualization and index-of-refraction model

MHz rate flow visualization

The MHz rate flow visualization system has been described and demonstrated elsewhere (Thurow et al., 2002a&b) so only a brief description will be given here. The system consists of a pulse burst laser and an ultra high-speed CCD camera. The pulse burst laser is

described by Lempert et al. (1996, 1997), Wu et al. (2000), and Thurow et al. (2002a&b). It is a custom-built 2nd generation Nd:YAG laser system that achieves a high repetition rate through the use of a continuous wave (cw) oscillator, a dual Pockel's cell pulse "slicer", and a series of flashlamp-pumped amplifiers. The fundamental output is frequency doubled to 532 nm (green). The laser can create between 1 and 99 pulses over a time span of approximately 150 microseconds and can operate at a maximum rate of 1 MHz. Recently, a phase conjugate mirror was incorporated into the laser system that allows for higher energy levels than those reported in previous publications. A typical burst of pulses in this work consists of 17 pulses (~5 nsec duration each) with inter-pulse timing of 4 microseconds and an average power of ~10-15 mJ/pulse.

The ultra high-speed CCD camera used in conjunction with the laser is manufactured by Dalsa Corp. (Model 64K1M). The camera uses a CCD chip masking technique to acquire 17 consecutive images at high speeds with a maximum rate of 1 MHz. The camera has a fill factor of less than 3% and a resolution of 245 x 245 pixels. The extremely low fill factor and a non-rectangular pattern of active pixels do not cause major problems for flow visualization, but makes the camera unsuitable for the use in a SH wavefront sensor discussed in Sec. III.

For flow visualization, the laser beam is formed into a sheet and passed through the flow to visualize a slice of the flow field. Seeding is provided using the product formation technique where water contained in the warm, moist, ambient air condenses upon entrainment into the jet and mixing with the cold, dry air of the jet core. Concerns about the size of the particles formed and the response time of their formation have been previously addressed, and the particles are believed to accurately mark the features of the shear layer (Elliott et al., 1992).

The flow field under consideration in this paper is a Mach 1.3 ideally expanded rectangular jet of aspect ratio 3. The exit dimensions of the converging-diverging nozzle are 38.1 x 12.7 mm (1.5" x 0.5"). The diverging contour within the nozzle was designed using the method of characteristics for uniform flow at the exit. Figure 2 illustrates the experimental set-up and orientation of the laser sheet (other components are discussed in Sec. III).

Figure 3 is a set of 4 images (out of 17 total) acquired with the above set-up. Flow is from left to right and the bright regions correspond to areas where moisture in the entrained ambient air has condensed in the mixing layer; only the mixing layer is being visualized. The vertical lines indicate the location of a HeNe laser beam that was used with the SH wavefront sensor and will be discussed in more detail in Sec III.

The images span the region from 5 7/8 jet heights (x/h) to 10 13/16 x/h . In the images, large-scale structures can be identified and are organized in an asymmetric pattern. At this streamwise location, the large-scale structures are on the order of 15-25 mm in size.

Spatial and temporal development of structures can be noted between the images. For example, a large-scale structure can clearly be seen in the lower half of the mixing layer. In the first frame, the structure is intersected at its midsection by the two vertical lines marking the passage of the HeNe beam through the flow. Immediately before and after the structure, braids can be seen that likely connect the structure to others. In subsequent frames, the structure convects downstream. A manual measurement shows the convection velocity to be ~270 m/sec. In addition to translation of the large-scale structure, many other changes can be observed. For example, the upstream braid region of the mixing layer is stretched and convoluted. In the 3rd image, a turbulence structure is seen protruding in the core flow as it rides on the top of the large-scale structure (lower half of mixing layer between the vertical lines). In the upper half of the mixing layer, immediately upstream of the vertical lines, a slight tear (or notch) can be seen in the 1st image. In the subsequent images, this tear progress into the vertical lines and becomes compressed between the structure developing behind it and in front of it. These features will be addressed again in Sec IV with consideration to their impact on a wavefront passing through them.

Index of refraction Model

In order to understand the influence of the flow field on a wavefront passing through it, a model is needed to relate the index of refraction field to the flow images. As stated in the introduction, the index of refraction is directly proportional to the density of the flow (see Eq. 2). The relationship between the images presented here and the density of the flow field is not straightforward. Thus, a model must be used to tie what is seen in the images to the density of the flow.

First, it must be considered what is actually being visualized in the images. The seeding technique used here is product formation and thus the presence of light-scattering particles in the flow will be a function of the amount of mixing between the jet and ambient air for a given location and time. This process is quite difficult to model, but it is generally assumed that the particles mark a large portion of the mixing layer. This is supported by PDF measurements made by Messersmith et al. (1991) and will be assumed to be the case in this work. It is also clear that neither the ambient air nor the jet core will be visualized with this technique. Thus, the portions of the image that do not display intensity will

be assumed to have a constant density and, therefore, a constant index of refraction.

In the experiments presented here, the ambient air (outside of the mixing layer) has a density of 1.14 kg/m^3 ($T=303 \text{ K}$) and an associated index of refraction (Eq. 2) of $n_{\text{amb}}=1.000254$. For the ideally expanded Mach 1.3 jet, the density within the jet's core is 1.52 kg/m^3 with a corresponding index of refraction of $n_{\text{core}}=1.000339$. Thus, the first part of the model assumes that flow outside of the mixing layer has an index of refraction of n_{amb} while inside the mixing layer (i.e. the jet core) has index of refraction equal to n_{core} .

Once the index of refraction values have been assigned for the ambient and core fluid, the index of refraction within the mixing layer must be determined. However, the index of refraction varies both temporally and spatially within the mixing layer. This issue has been explored by Dimotakis et al. (2001) in incompressible and compressible shear layers. In this work, they used a Rayleigh scattering technique to measure the density in the flow directly. They subsequently showed that the mixing layer can be represented using an index of refraction equal to the average value of the two bounding streams. Computed wavefronts using this average index value for the mixing layer were found to be nearly identical to the wavefront calculated using the exact density values throughout the mixing layer. For the case of a jet, this would correspond to $n_{\text{mix}}=(n_{\text{amb}}+n_{\text{core}})/2$. This approach is used in the current study.

Optical aberrations

Upon estimating the flow's index of refraction field, optical aberrations can be determined in terms of the beam's optical path length (OPL). The optical path length is defined as:

$$OPL(x, z) = \int_{y_1}^{y_2} n(x, y, z) dy \quad (3)$$

where the beam propagates in the $-y$ direction and $n(x, y, z)$ is the index of refraction field in three dimensions. The coordinate system has been chosen to conform to fluid dynamic conventions; therefore the z -axis does not correspond to the propagation direction of light. In the present case, the index of refraction field is only estimated in the x and y directions and thus only $OPL(x, z=z_0)$ can be calculated. It is more useful, however, to only consider the optical path difference (OPD), which is

$$OPD(x, z) = OPL(x, z) - \overline{OPL(x, z)} \quad (4)$$

where the overbar indicates the average value. The OPD is commonly normalized by the wavelength of the propagating light and thus given in waves or radians.

The overall index of refraction model and OPD calculation is demonstrated in Figure 4. Figure 4 contains an image of the flow (3rd image of Figure 3) on the left and the corresponding estimated index of refraction field on the right. In the index image, black corresponds to n_{amb} and white to n_{core} . The mixing layer is gray and corresponds to the average of the ambient and core indices. There are some regions where it appears the index of refraction was incorrectly assigned. This is due to the automated process, which is still under development. Within the vertical lines, the process worked quite well.

Immediately below the indexed image is the OPD calculated for the image by integrating in the y direction. The vertical lines through the image and the OPD indicate the portion of the wavefront measured using the SH wavefront sensor. In general, the OPD from the images increases in the x -direction as the mixing layer increases in thickness. As a measure of the level of fluctuations, the standard deviation of the entire OPD over 20 sets of 17 images is 0.478λ ($\lambda=632.8 \text{ nm}$). Over the 6 mm aperture indicated by the vertical lines, the standard deviation of the OPD is 0.132λ . Comparisons between the wavefront determined from the images and the SH sensor will be addressed in Sec. IV.

It should be noted that the OPD estimation of the wavefront only holds if one assumes a small angle approximation for light rays. In other words, the angle of propagation of light rays traveling through the mixing layer remains relatively constant throughout the mixing layer. This assumption is generally true over small distances and small index of refraction gradients, but has not been explicitly examined for this case.

III. MHz rate SH wavefront sensor development

SH wavefront sensor design

In a SH sensor, an optical wavefront is spatially sampled by a lenslet array that is typically organized in a rectangular or hexagonal pattern. Each lenslet in the array produces a focal spot on the recording medium with a lateral displacement corresponding to the local wavefront tilt. In order to produce an accurate wavefront measurement, the lenslet spacing must be sufficiently small so that the wavefront is well represented by the resulting piecewise linear approximation to the wavefront gradient. In addition, when this criterion is met the focal spots produced by each lenslet will be nearly diffraction limited.

The radius of each spot is given by Equation 5,

$$r_{\text{SPOT}} = \frac{4 \cdot \lambda \cdot f}{\pi \cdot \Delta} \quad (5)$$

where λ is the wavelength, f is the focal length of each lenslet, and Δ is the lenslet diameter. Significant distortions of the focal spots can be caused if the wavefront varies significantly over distances on the order of Δ .

A high speed CCD camera records images of the array of focal spots. Accurate measurements of spot locations result in a discretized measurement of the wavefront gradient. The smallest wavefront gradient that can be measured is given by Eq.6,

$$\theta_{MIN} = \frac{\delta x}{f} \quad (6)$$

where δx is the uncertainty in the measured spot displacement. Clearly, the sensitivity of the wavefront measurement is proportional to the uncertainty in the spot location and to the inverse of the focal length since a large f results in a larger spot displacement for a given wavefront tilt.

The spot displacement is measured using an automated process. In our approach, which is typical of many SH systems, the brightest pixel behind a given lens aperture is taken to be an approximate spot centroid. This centroid estimate is then refined by fitting the spot intensity pattern to a two dimensional Gaussian distribution. The fitted center of the Gaussian is then taken to be a measure of the spot location. Two dimension sinc^2 patterns, which correspond to the actual diffraction pattern behind a square aperture, were also used as fitting functions, but it was determined experimentally that the Gaussian gave equally accurate results with less computational effort. It is our experience that a spot center can be located to within a tenth of a pixel if the spot covers at least 4 pixels in the horizontal and vertical directions.

The maximum wavefront tilt that can be measured reliably is set by the practical constraint that focal spots should not move from behind their corresponding lenslet aperture. Here the maximum displacement would put the edge of the spot along the edge of the boundary behind the microlens array. This limitation assures that adjacent spots will never travel past each other. This constraint allows each focal spot to be consistently identified with its corresponding aperture in a straightforward, automated manner. In most cases, the first term in Equation 7 will dominate since the lenslet size will be much larger than focal spot size.

$$\theta_{MAX} = \frac{\Delta}{2 \cdot f} - \frac{4 \cdot \lambda}{\pi \cdot \Delta} \approx \frac{\Delta}{2 \cdot f} \quad (7)$$

Combining Equations 6 and 7 we can develop an expression for the dynamic range of a SH sensor.

$$\theta_{MAX} - \theta_{MIN} = \frac{1}{f} \left(\frac{\Delta}{2} - \delta x \right) \quad (8)$$

This equation shows that in the absence of any other constraints, SH designs are driven to use lenslet arrays with short focal lengths.

The recording media used determines the SH's temporal resolution. In order to measure time resolved wavefront data, a very high speed CCD is needed. Design tradeoffs in high speed CCD's result in low fill factors, large pixels, and low resolutions. The low fill factors are due to the use of area adjacent to pixels for data storage. Large pixel sizes are needed to capture sufficient numbers of photons during short exposures.

The CCD camera used in this work was a Princeton Scientific Instruments (PSI) Ultra Fast CCD camera. This camera has a maximum frame rate of 1 MHz, and can capture up to 28 frames. The high frame is achieved using a specially manufactured CCD chip, which contains 28 on-chip storage bins next to each pixel. The charge in each pixel can be very quickly shifted to the local memory and read out after acquisition of a complete set of 28 images. The camera's resolution is 82 x 161 pixels. Each pixel and associated memory cells is 115 μm square and arranged in a standard rectangular grid pattern. The relative positioning of memory cells and active pixels provides the camera with a 50% fill factor in one dimension while maintaining ~100% fill factor in the other direction.

The large pixel pitch, low resolution, and low to moderate fill factor of this camera makes the design of an efficient SH sensor particularly difficult. In order to achieve subpixel resolution for spot center location, the spots must have a diameter of at least four pixels. This drives the design towards the use of very large $f/\#$ microlenses.

In order to estimate the magnitude of the wavefront variations in our flow, preliminary experiments were performed by using a 1 meter focal length lens, to focus a narrow (~0.7 mm) HeNe beam onto the PSI camera. This beam passed through the shear layer and the resulting spot displacement on the camera CCD was recorded. These single aperture experiments indicated that a spatial sampling of ~1mm would provide the resolution needed to ensure all spots formed were nearly diffraction limited. In addition, the measured wavefront tilts were on the order of 100 μrad .

With this knowledge in hand, a suitable microlens array was selected from those that were commercially available. The microlens chosen was a square array with a pitch of 1.06 mm and a focal length of 260 mm. This microlens array is a stock item from Adaptive Optics Associates, model 1060-260-S-B. Larger $f/\#$ microlens arrays were not stocked. In order to further increase spot size and wavefront sensitivity, a negative lens was placed against the micro-lens array increasing its equivalent focal length to approximately 350 mm. The resulting focal spot radius was approximately 270 μm , ensuring that we were able to determine the spot

centers with subpixel accuracy. In this configuration our SH provides the ability to measure wavefront tilts ranging from 33 μrad to 750 μrad in either direction.

Wavefront Reconstruction

The displacement of each focal spot is determined by a MATLAB script that fits every focal spot to a Gaussian intensity pattern. The user clicks on the initial spot locations and the program then fits each spot in every subsequent frame. An image of the spot pattern taken with no flow is used to determine the zero wavefront aberration location of every focal spot.

Once the spot displacements are determined, Equation 1 is used to form a discretized version of the wavefront gradient,

$$\vec{S}_{i,j} = \nabla\phi(x_i, y_j) \quad (9)$$

where $\vec{S}_{i,j}$ is an $N \times M$ array of measured wavefront gradient vectors at the i,j lenslet location.

We reorder $\vec{S}_{i,j}$ by grouping all of the x and y components of the gradient measurements together to form a new vector s_i . The continuous gradient operator in Equation 9 is approximated by second order finite differences. In the interior of the spot pattern, centered differences are used. Discrete representations of the gradient operator on the boundary of the spot array require the use of one sided finite difference approximations. For example, Equation 10 relates the x-component of the wavefront gradient to two adjacent wavefront values. Equation 11 shows the approximation to the wavefront slope x-component for a left edge point.

$$\frac{\partial\phi(x, y)}{\partial x} \approx \frac{\phi(x+h, y) - \phi(x-h, y)}{2 \cdot h} \quad (10)$$

$$\frac{\partial\phi(x, y)}{\partial x} = \frac{-3 \cdot \phi(x, y) + 4 \cdot \phi(x+h, y) - \phi(x+2 \cdot h, y)}{2 \cdot h} \quad (11)$$

Assembling the finite difference approximations for every measured s_i , we can form a matrix approximation to the ∇ operator shown in Equation 12 where ϕ_j is a vector of wavefront values measured at the center of each lenslet aperture.

$$s_i = A_{ij} \phi_j \quad (12)$$

Equation 12 is an overdetermined system since the vector s_i contains $2 \times N \times M$ numbers while there are

only $N \times M$ values of ϕ_j . This relationship is solved by multiplying both sides by $(A^T A)^{-1} A^T$.

$$(A^T A)^{-1} A^T s_i = (A^T A)^{-1} A^T A \phi = \phi \quad (13)$$

Often, the matrix $A^T A$ is ill-conditioned so singular value decomposition (SVD) is used to compute a pseudo-inverse. This procedure is equivalent to solving for the ϕ_j that is the least squares solution to Equation 12 (Press et al., 1992).

It should be noted that the constant part of the wavefront aberration can not be measured by a SH wavefront sensor. As a result, the reconstructed wavefronts are normalized typically by subtracting the average of the wavefront, $\bar{\phi}_j$.

Using the reconstructed wavefront and A_{ij} the spot displacements can be computed and compared to the measured values. A comparison of the displacements computed from the reconstructed wavefront and the measured displacements are shown in Figure 5. For this figure all displacements have been enlarged by a constant factor in order to make a visual comparison easier. It is clear that the reconstructed wavefront produces nearly the same spot displacements as were actually measured.

Experimental Shack-Hartmann Measurements

The experimental setup of the SH is shown in Figure 2. The SH measured the wavefront distortions imposed upon a HeNe laser beam after it passed through a Mach 1.3 rectangular jet flow. The HeNe laser was spatially filtered and expanded so that the diameter was approximately 30 mm. The beam was slightly wider than the diagonal measurement of the PSI camera CCD chip.

A 4-f lens system is used to relay the wavefront just after it exits from the jet flow onto microlens array. This relay system removes the effects of diffraction as the beam propagates to the wavefront sensor. In addition, the relay system allows the SH sensor to be located at a convenient distance away from the flow. Placing the SH adjacent to the jet could alter the flow or lead to vibration of the optics.

The collimation of the HeNe probe beam was carefully checked where it passed through the jet and where it was imaged onto the SH microlens array. Small amounts of misalignment, however, are unimportant since the SH system only measures relative aberrations between the flow on and off states.

Neutral density filters were used at the HeNe to adjust the intensity of the beam so that the focal spots were almost saturated. A 633 nm bandpass filter was used at the PSI camera to block any stray light.

Observations from this experiment show that most spots produced were diffraction limited while some exhibited slight distortions, thereby implying an adequate spatial resolution had been used.

Unfortunately the camera used in this study has a defective CCD chip where a large number of the pixels (on the order of 10-20%) are useless. The defective pixels, however, are grouped on one half of the chip. Thus, for this study, only half of the CCD chip (an 82 x 82 pixel region) is used for the SH sensor. We are currently investigating whether or not more of the chip can be used in future experiments.

The 82 x 82 pixel usable region of the CCD chip corresponds to a sensor area of 9.4 x 9.4 mm. Depending upon spot size and motion, this allows the sensor to image an 8 x 8 pattern of spots using the current microlens array. For this study, only a 6 x 6 spot pattern was used. This was chosen to avoid erroneous tracking of spot centers when the spots moved close to the edge of the CCD and also to circumvent some additional noise that occurred along the edges of the CCD. More accurate alignment may be used in future experiments to ensure the edge spots remain on the CCD. The vertical white lines in Figure 4 outline the passage of the HeNe beam that corresponds to the measured wavefront.

The reconstructed data consists of a 6 x 6 matrix of scalar values corresponding to the wavefront. Some examples of measured wavefronts obtained at 500 kHz are shown in Figure 6. The wavefronts in Figure 6 have been smoothed using a bi-cubic interpolation scheme. In addition, the mean value of ϕ has been subtracted to yield only the relative wavefront since piston cannot be determined.

Despite the use of a rectangular nozzle the wavefronts produced possessed a high level of two-dimensionality as can be seen in Figure 6. Typical fluctuations within the wavefronts were on the order of 1/3 waves, while some distortions larger than 2 waves were observed. Manual measurements taken on sequential wavefronts show that features within the wavefront possessed a downstream velocity of 200-300 m/s, similar to the measured convective velocity of structures observed in the flow.

IV. Simultaneous flow visualization and wavefront sensing

In this section, the measurements obtained with the SH wavefront sensor are compared to the calculated wavefronts from the images. Figure 2 shows the experimental set-up used to simultaneously acquire the

data. The laser sheet had to be directed and passed through the flow at approximately a 10 degree angle relative to the HeNe laser beam. Alignment between the laser sheet and the sampled portion of the HeNe wavefront was conducted using a circular aperture mounted 63.5 mm (2.5") above the center of the jet. Unfortunately, while this method insures alignment of the two beams at the position of the circular aperture, it does not ensure alignment throughout the entire flow field. Due to the close proximity of the aperture to the flow, however, alignment between the two beams is felt to be reasonable, but not optimal. A different method of alignment will be used in the future to ensure better accuracy.

The SH wavefront sensor is capable of recording 28 time correlated wavefronts while the flow visualization system can capture only 17 images, as each one used a different CCD camera. In order to make as efficient use of both systems as possible, the SH wavefront sensor was operated at 500 kHz and the flow visualization system at 250 kHz. Thus, there are two measured SH wavefronts for every flow visualization image. The timing between the two systems was arranged so that the 1st flow visualization image was measured simultaneously with the 2nd SH wavefront. The 2nd flow visualization image corresponds to the 4th SH wavefront and so on. There is no SH wavefront measurements available for the last 3 flow visualization images.

The four images of Figure 3 were taken simultaneously with the four wavefronts shown in Figure 6 and thus direct comparisons can be made between the two figures. Beginning with the 1st image and only paying attention to the fluid within the vertical lines, we notice that inner and outer boundaries of the mixing layer are relatively flat (in comparison with the 3rd or 4th image). This is especially true at the inner boundaries. The corresponding wavefront measured by the SH sensor and shown in Figure 6 is also relatively flat (in comparison with the 3rd and 4th wavefronts). A similar observation can be made for the 2nd image of Figure 3 and 2nd wavefront of Figure 6.

In the 3rd image, the interface between the core fluid and the mixing layer is much more convoluted with sharp and well-defined features. In the upper half of the mixing layer, a tear at the rear of a large-scale structure has progressed to within the two vertical lines. In the lower half of the mixing layer, a smaller scale structure protrudes from the large-scale structure into the jet core. These features are also on the same scale as the wavefront passing through them. In the corresponding wavefront of Figure 6, the wavefront is more deformed than in previous realizations and quite three-dimensional. A similar trend can be noticed in the 4th image and wavefront respectively as the notch in the large-scale structure of the lower half of the mixing

layer has progressed into the line of sight of the wavefront sensor. In response, the measured wavefront appears to exhibit a higher degree of variation.

Qualitatively, there appears to be a good match between the gross features of the measured wavefront and the features of the mixing layer responsible for the aberrations. When the mixing layer appeared smoother and devoid of turbulence features on the same scale as the wavefront, the wavefront appeared to be less perturbed. On the other hand, when the mixing layer interface was more undulating, the measured wavefront also appeared more undulating.

The analysis to this point, however, has been quite subjective and preliminary. Quantitative data is needed to correlate the features of the flow to the aberrated wavefront. This can be done using the index of refraction model discussed in Sec. II to calculate the OPD of a wavefront passing through the flow. The OPD can then be directly compared to the wavefront measured by the SH sensor as described in Sec. III.

This comparison is shown in Figure 7. Each graph displays the 1-D wavefront calculated from the images and a 1-D slice through the wavefronts measured by the SH sensor. The broken line corresponds to the image based estimated wavefront while the solid line corresponds to the SH sensor measured wavefront. The 1-D wavefronts in Fig. 7 are a streamwise slice taken from the 2-D SH data taken at a location corresponding to the intersection between the laser sheet and the sampled HeNe beam.

For each of the four realizations, the matching between the two curves varies greatly. For the first two plots, there is some agreement, but overall the matching is poor. In agreement with the qualitative analysis, the variations are not as large as in other instances and both wavefronts have a similar magnitude of variations. On the other hand, the shapes of the aberrations are quite different. This could quite possibly be due to a misalignment between the flow visualization laser sheet and the optical wavefront propagating through the flow. The measured wavefronts of the SH sensor are quite three-dimensional and any minor misalignment could have a major impact on the comparison. It is also possible that the model for calculating the OPDs from the images needs improvement and does not accurately model the propagation of wavefront through the flow.

The 3rd plot, however, shows a good match between the image calculated and the SH measured wavefront. Both the shape and magnitude of the aberrations match up well. The 4th plot also shows a good match in terms of shape, but there appears to be a shift in relative position between the two peaks. In this case, the flow exhibited some larger scale features at the same scale as the sampled wavefront.

An indication of the quality of match between the image calculated wavefront and the SH sensor

measured wavefront can be found by subtracting one wavefront from the other. Ideally, if the wavefronts matched exactly, this would reduce the subtracted wavefront to zero. For the full sequence of 14 image/SH sensor wavefront pair, the standard deviation is reduced to 0.1348 from 0.1646 when the image calculated wavefront is subtracted from the measured wavefront. Thus there appears to be some overall agreement between the two waveforms.

Clearly these results are quite preliminary and point to a need for improvements in the technique. The best match between the flow visualization and the SH sensor occurred when the flow had a very distinguished feature within it (the protruding structure in the lower half of the mixing layer). In other cases, however, the match was not very good. Similar results were noted in 19 other simultaneous data sets. The next section will discuss a number of action items that will be taken to improve the overall process and to obtain a higher quality set of data.

V. Optimization of technique and future plans

The results presented here are very preliminary and designed to test and validate the experimental techniques used. At this point, the temporal resolution of the technique has not been exploited with images and wavefronts being analyzed on an individual basis. Better agreement is needed between the flow visualization and measured wavefronts before the advantages of time resolved series can be fully utilized. Based on the preliminary results of this paper, the next set of experiments will incorporate a number of changes and improvements that should result in a much higher quality set of data. Listed below are some of the areas identified for improvement that will be incorporated in future work.

1.) *Increase the sampled wavefront size relative to flow field.* The sampled portion of the wavefront only measured $6 \times 6 \text{ mm}^2$ while the large-scale structures in the flow are on the order of 15-25 mm in the streamwise direction. Thus, the measured wavefronts do not fully capture the effects of large-scale structures in each snapshot. However, it does capture these effects in successive image, due to the real-time nature of the current technique. Using large sampled wavefront size would greatly improve the performance of the index of refraction model for the flow visualization images as the region of interest in the flow would be resolved by a greater number of pixels. A larger sampled wavefront can be achieved by placing a telescope between the flow and the lenslet array. The addition of the telescope will have the additional benefit of magnifying the wavefront tilts resulting in a larger displacement of

spots on the CCD array and therefore a better measurement of the local tilt.

2.) *Make more efficient use of the PSI camera's CCD chip.* Currently, only half of the PSI's CCD chip is being used in the SH wavefront sensor to calculate wavefronts. A 6 x 6 grid of spots is contained on an 82 x 82 pixel portion of the chip, although the chip is 161 x 82 in size. This is because of a substantial amount of damage contained on one half of the chip. There is a row of approximately 10 pixels below the damaged area, however, that is not damaged and could yield useful information. Through proper alignment, this 10 x 161 region of undamaged pixels could be aligned with the laser sheet allowing for increased aperture and resolution of the wavefront coincident with the laser sheet flow visualization. Thus, the SH would measure a 2-D wavefront in the 82 x 82 good portion of the chip and measure an additional 1-D component along the 10 x 161 portion of the chip.

3.) *Use a lenslet array with smaller lenslets.* The current lenslet array has a 1.06 mm pitch. Since the good portion of the PSI CCD chip is ~8 x 8mm, only a 6 x 6 grid of spots was formed. With a smaller pitch, the same wavefront can be resolved into many more spots. Recently, we have obtained an array with 400 micron pitch, which should allow for a 15 x 15 grid of spots on the same region of the CCD chip. As discussed in Sec. III, there is a limit to the number of spots that can be formed on the chip before they begin to overlap. This also will be examined further.

4.) *Use a better method for aligning the laser sheet flow visualization with the SH wavefront sensor.* The technique used in this paper consisted of aligning the two beams at a single location. Unfortunately, this method of alignment does not ensure that the beams are traveling parallel to each other through the flow field. Especially for a small SH viewing aperture, misalignment could cause significant mismatch between the image calculated and SH measured wavefronts. A better method of alignment would involve using apertures (or knife edges) at various points along the propagation direction. Thus, the laser sheet and the HeNe laser beam could be adjusted to be perfectly parallel through the flow field. This should significantly improve the matching between wavefronts.

5.) *Try different models for determining the index of refraction field from the flow field images.* The current method of determining the index of refraction is based on a rather simple model and does not incorporate any detailed knowledge about the relationship between the product formation seeding technique and the mixing

layer. Some of the assumptions involved need to be examined further. Furthermore, it is currently assumed that the light passing through the mixing layer will only refract at a small angle. This assumption needs to be evaluated more rigorously. Other areas of improvement related to the model include alignment of the image with the propagation direction of the wavefront as well as increasing the magnification of the imaging system to better resolve the region of the flow coincident with the measured optical wavefront.

6.) *Use a cross-stream laser sheet as well as a streamwise laser sheet.* The advantage of a streamwise laser sheet is that it is aligned with the direction of the flow and therefore structures can be followed through the images. The disadvantage, however, is that the shape of the structures is not known in three dimensions, so only a 1-D wavefront can be calculated for each image. A cross-stream sheet, on the other hand, allows for a view of structures in the spanwise direction and thus reveals more details about their three-dimensionality. As the flow is moving into the sheet, a three-dimensional view of the mixing layer can be reconstructed from each successive slice through the mixing layer using the real-time capability of the current imaging system. This reconstruction would require some additional modeling efforts to determine the best method of reconstruction, but should be very useful in giving a three-dimensional portrait of the turbulence structures and should allow for more direct comparisons between the two-dimensional wavefronts measured by the SH sensor and the flow visualization.

7.) *Conduct identical experiments using single-shot, high resolution cameras.* A limitation to the current data is the lack of a baseline case for comparison. The quality of data obtained from flow visualization and the SH sensor are limited by the modest spatial resolution of the Dalsa and PSI cameras, respectively. Furthermore, the nature and trend of the results are not known. High resolution cameras used in the place of the high-speed cameras should yield higher quality data, albeit without any time information. This higher quality data could then be used to develop a better model for the index of refraction of the flow visualization images and better algorithms for determining the center of spots on the SH sensor. The data would also be used to establish expectations for the measured wavefronts and determine sources of error by comparing the data between the high-speed systems and high resolution systems.

VI. Conclusions

The results presented here are quite preliminary. Still, a number of conclusions can be drawn from this

work. First, the feasibility of a system to measure optical aberrations simultaneously with the flow at MHz rates is clearly demonstrated. The MHz rate flow visualization described in Sec. II is quite useful for following the evolution of structures while the SH wavefront sensor described in Sec. III can measure two-dimensional wavefronts at a MHz rate.

Qualitatively, the simultaneous results seemed to indicate correlated features. When the flow appeared jagged within the sampling window, the wavefront appeared more distorted. Conversely, when the flow appeared to be less undulating, the wavefronts also appeared to be smoother.

Quantitatively, the wavefronts calculated from the flow visualization images differed by varying degrees from the wavefronts measured with the SH sensor. In some instances, the comparison was quite good; however, in other instances it was quite poor. A number of issues, however, may contribute to this lack of agreement.

Future experiments will be conducted in a similar manner, but will take into account a number of lessons learned from this preliminary set of experiments in Sec. V.

Acknowledgements

The support of this research by the Dayton Area Graduate Studies Institute DAGSI and AFRL is gratefully acknowledged. Fruitful discussion with Mike Stanek of AFRL is very much appreciated. The first author would like to thank the Department of Defense for his National Defense Science and Engineering Graduate Fellowship

References

- P. E. Cassady, S. F. Birch and P. J. Terry, "Aero-optical analysis of compressible flow over an open cavity," AIAA J., **27**, 758 (1989).
- P.E. Dimotakis, H. J. Catrakis and D.C. Fourquette, "Flow structure and optical beam propagation in high-Reynolds-number gas-phase shear layers and jets," J. Fluid Mech., **433**, 105, (2001).
- G. S. Elliott, M. Samimy and S. A. Arnette, "A study of compressible mixing layers using filtered Rayleigh scattering," AIAA Pap. 92-0175 (1992).
- E. J. Fitzgerald and E. J. Jumper, "Scaling aerodynamic aberrations produced by high-subsonic-Mach shear layers," AIAA J., **40**, 1373 (2002).
- R. J. Hugo, E. J. Jumper, G. Havener and C. Stepanek, "Time-resolved wave front measurements through a compressible free shear layer," AIAA J., **35**, 671 (1997).
- E. J. Jumper and E. J. Fitzgerald, "Recent advances in Aero-optics," Preprint submitted to Elsevier Preprint. (2002) Need to update
- W. R. Lempert, P. F. Wu, B. Zhang, R. B. Miles, J. L. Lowrance, V. J. Mastocola, and W. F. Kosonocky, "Pulse burst laser system for high-speed flow diagnostics," AIAA Pap. 96-0179 (1996).
- W. R. Lempert, P. F. Wu, and R. B. Miles, "Filtered Rayleigh scattering measurements using a MHz rate pulse-burst laser system," AIAA Pap. 97-0500 (1997).
- N. L. Messersmith, J. C. Dutton and H. Krier, "Mie scattering measurements of scalar probability density functions in compressible mixing layer," AIAA Pap. 91-1686 (1991).
- L. McMackin, B. Masson, N. Clark, K. Bishop, R. Pierson and E. Chen, "Hartmann wave front sensor studies of dynamic organized structure in flowfields," AIAA J., **33**, 2158 (1995).
- W. Press, S. Teulolsky, W. Vetterling, and B. Flannery, *Numerical Recipes in C: The art of Scientific Computing* 2nd Ed. Cambridge University Press 1992
- B. Thurow, J. Hileman, M. Samimy and W. Lempert, "Compressibility effects on the growth and development of large-scale structures in an axisymmetric jet," AIAA Paper 2002-1062 (2002a).
- B. Thurow, J. Hileman, W. Lempert and M. Samimy, "A technique for real-time visualization of flow structure in high-speed flows," Phys. Fluids, ??? (2002b).
- P. F. Wu, W. R. Lempert, and R. B. Miles, "MHz pulse burst laser system and visualization of shock-wave/boundary layer interaction in a Mach 2.5 wind tunnel," AIAA J. **38**, 672 (2000).

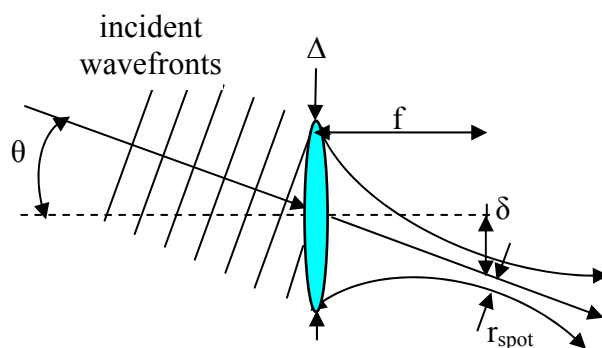


Figure 1 - Schematic of wavefront tilt measurement with a single lenslet.

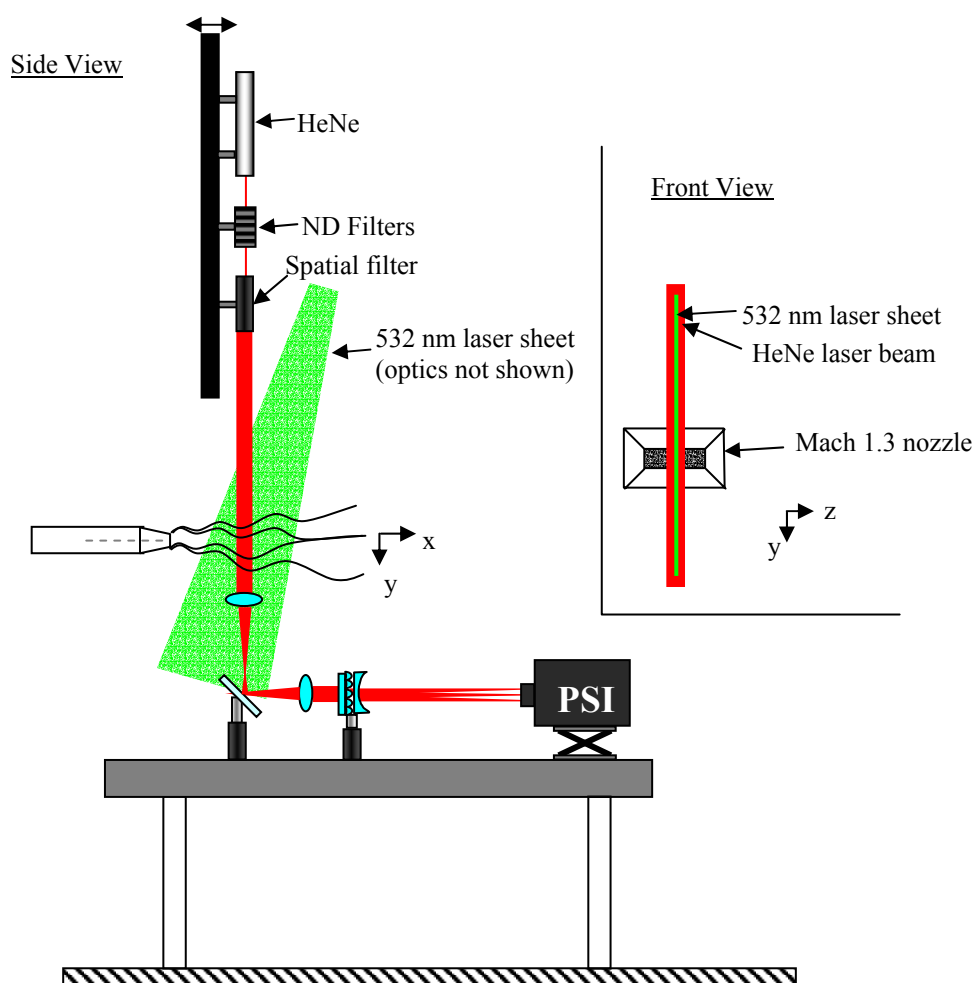


Figure 2 – Schematic of experimental set-up.

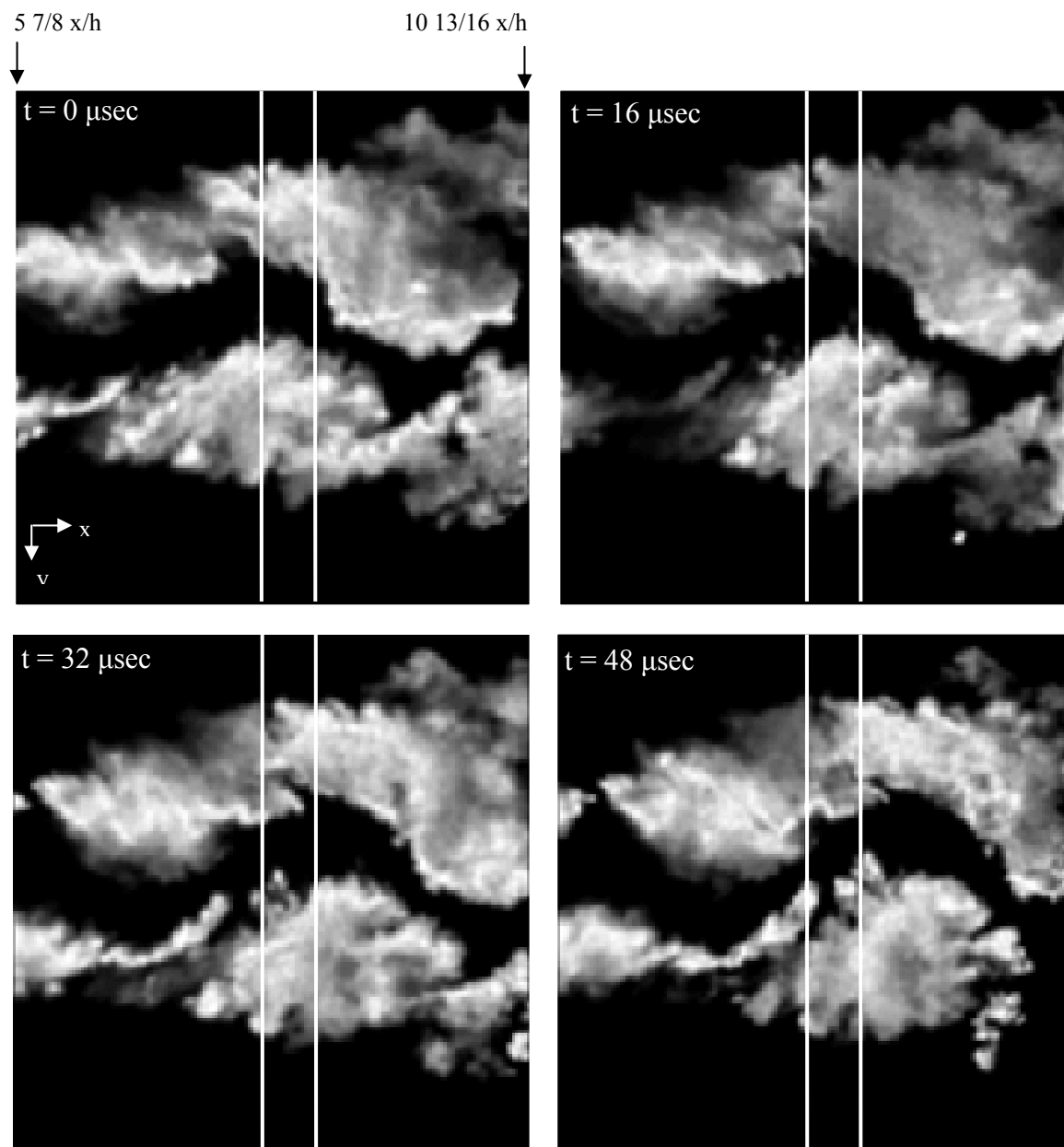


Figure 3 – Sequence of four images (out of 17) of a Mach 1.3 rectangular jet. Vertical lines show the location of the HeNe laser beam relative to the flow and the location of optical wavefront measurements.

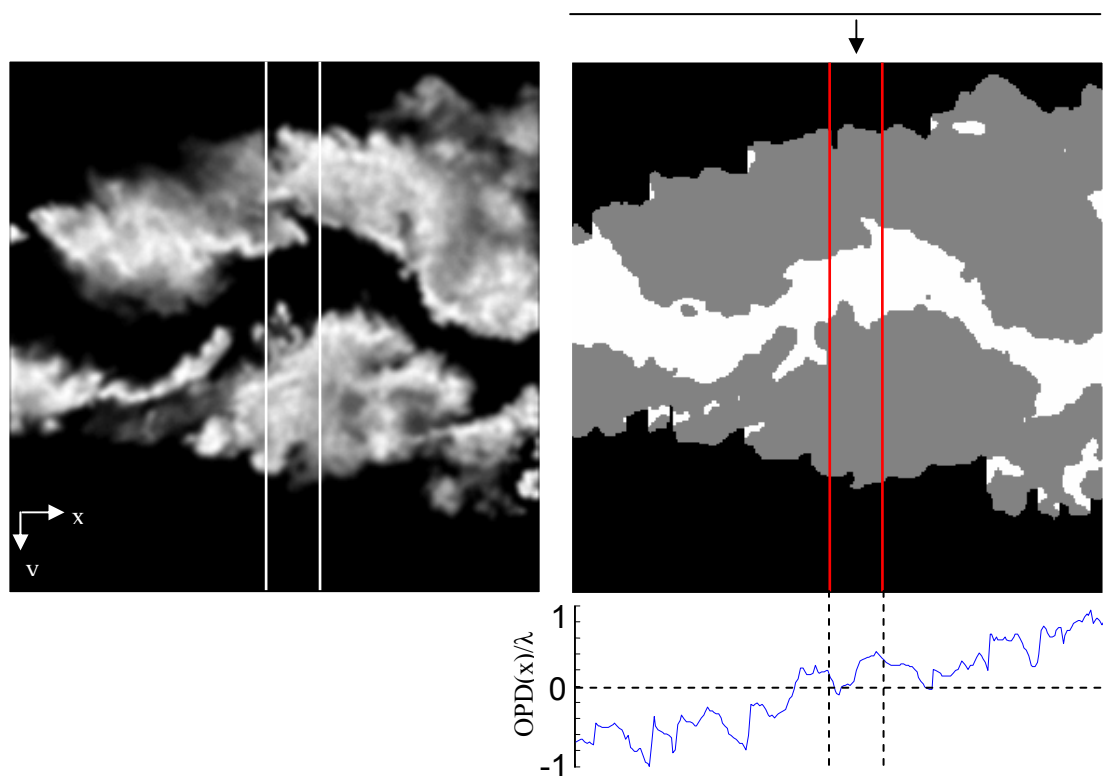


Figure 4 – Example of index-of-refraction model and calculated OPD from model.

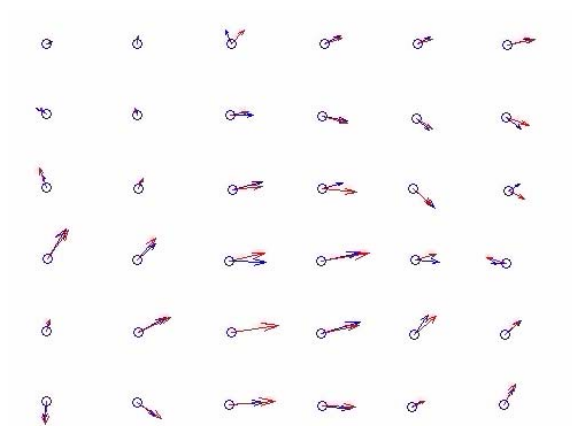


Figure 5 – Comparison of measured displacement vs. reconstructed displacement. (Blue – Measured/Red – SVD/circles – No aberration)

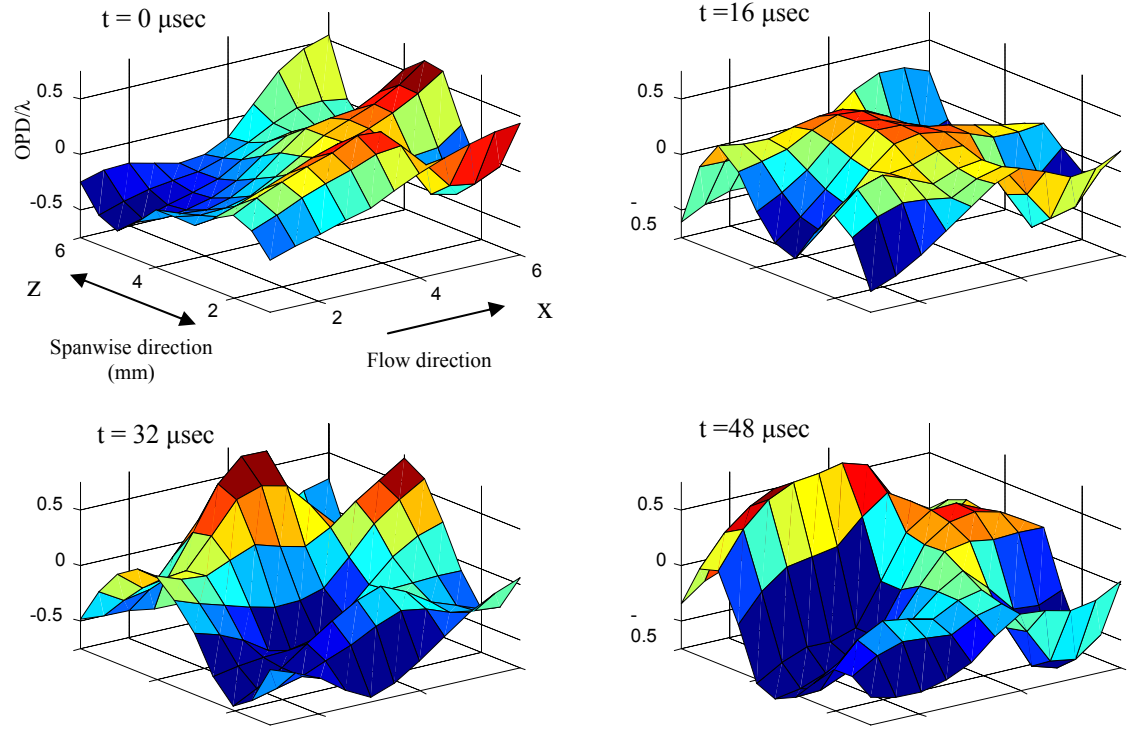


Figure 6 – Four measured wavefronts from Shack-Hartmann wavefront sensor. Wavefronts measured simultaneously with images of Figure 3.

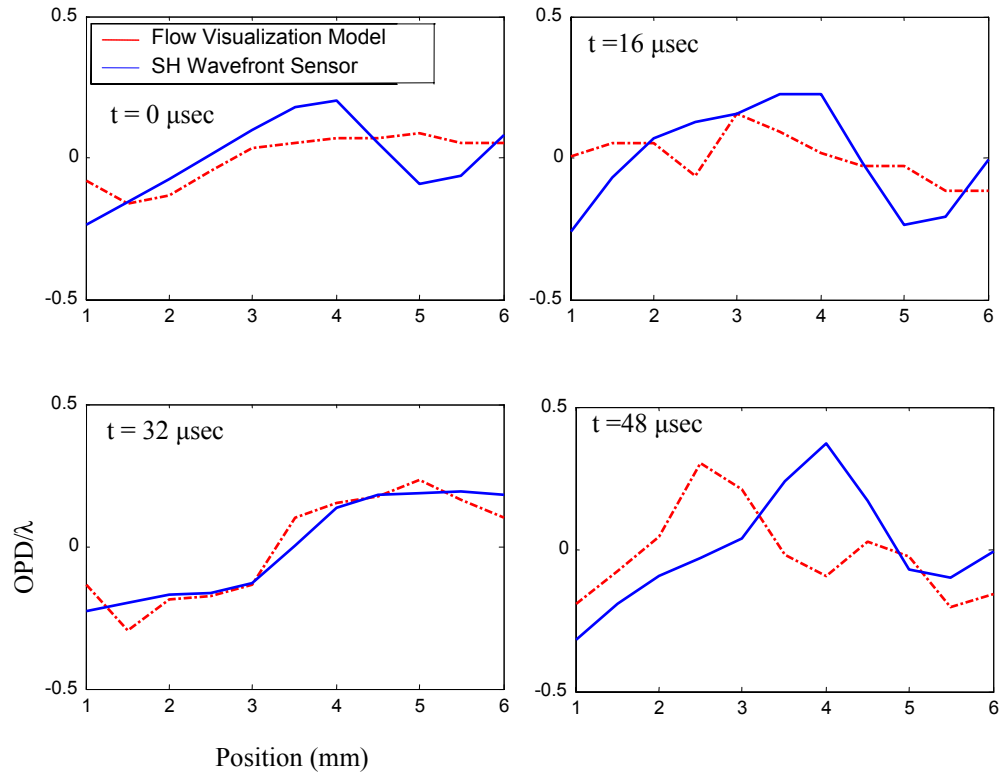


Figure7 –Comparison between wavefront calculated from flow visualization images and wavefront measured using SH wavefront sensor.